# A Charge Parity Ammeter

Nicholas J. Lambert,* Megan Edwards, Chiara Ciccarelli, and Andrew J. Ferguson*

Cavendish Laboratory, J. J. Thomson Avenue, Cambridge CB3 0HE, United Kingdom

ABSTRACT: A metallic double dot is measured with radio frequency reflectometry. Changes in the total electron number of the double dot are determined via single electron tunnelling contributions to the complex electrical impedance. Electron counting experiments are performed by monitoring the impedance, demonstrating operation of a single electron ammeter without the need for external charge detection.

KEYWORDS: *Single electron devices, Sisyphus impedance, Single electron ammeter, Radiofrequency reflectometry*
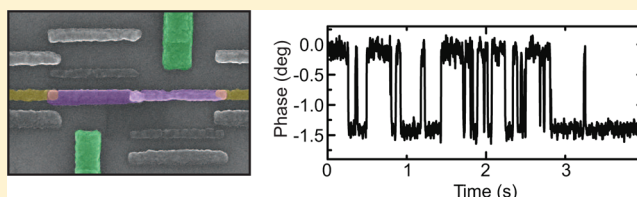
Single electron ammeters count each individual electron that passes. They enable the detection of tiny ($I < $ aA) currents[1] and show the real-time dynamics of single electron tunnelling.[2,3] They are, therefore, of use in efforts to redefine the ampere,[4−8] as they allow direct monitoring of the current produced by charge pumps and exploration of pump error mechanisms.[9] For example, the interaction between two independent charge pumps has been monitored by detecting the charge on an intermediate island, demonstrating feedback resulting in phase locking,[10] and charge sensing techniques have also probed the capture statistics for a dynamic quantum dot pump.[11] Furthermore, architectures allowing accurate (1 part in 10^8) current sources to be built from relatively imprecise pumps by the inclusion of electron counting devices have been proposed.[12]

These devices are made possible by high-sensitivity, high-bandwidth charge detection that can register the passage of an electron through a single electron device. Typically the charge detector employed is the single electron transistor[13] or quantum point contact,[14−16] which may be operated in a radio frequency impedance matching circuit to increase both bandwidth and sensitivity.[17−19] By using a double quantum dot and an asymmetrically coupled point contact charge sensor,[20] the direction of the flow of electrons can be monitored.

In this Letter, we demonstrate a double dot device in which external electrometry is unnecessary, simplifying the fabrication of a single electron ammeter. Rather, the internal tunnelling processes within a metallic double dot can be used to herald the passage of single electrons through the system, so the double dot acts as its own electrometer. Specifically, we demonstrate real-time measurements of the relative charge parity of the metallic double dot by probing the complex impedance of the device itself.

When any of the capacitors in a single electron device is driven by an alternating potential, periodic tunnelling of electrons can occur, resulting in an alternating current. For example, if an alternating potential is applied to the gate of a single electron box, a current is periodically driven across the tunnel barrier. If the drive frequency is sufficiently high that electron tunnelling does not happen adiabatically, energy is dissipated each half cycle leading to an effective resistance[21]—the "Sisyphus resistance". In general, the driven tunnel current is not in phase with the applied alternating potential and both real and imaginary components of the Sisyphus effect need to be considered.[22−24] In this Letter, we refer to the real and imaginary Sisyphus impedances as Z_S^{Re} and Z_S^{Im}, respectively. They are measured here by their dissipative and dispersive effects on a radio frequency resonant circuit. They can be observed in any single electron system; in this sense, they are dissimilar to the "quantum capacitance" which arises because of the change in bandstructure curvature close to an anticrossing between two levels, which is present in, for example, Cooper pair boxes[25] and double quantum dots.[26,27]

Our metallic double dot (Figure 1a) is defined by multiple angle shadow mask evaporation.[28] It comprises two microscale aluminum islands in series, with each island capacitatively coupled to an electrostatic gate, allowing individual control of their chemical potentials. The two islands are separated from each other by a nanoscale alumina tunnel barrier created by controlled oxidation. In previous experiments, we find this to give a barrier resistance of order 30 kΩ for junctions of this size. Aluminum source and drain leads allow electrical contact to the islands. We fabricate samples with both low and high lead-island tunnel junction resistances (here, called LR and HR devices). The LR device has a total resistance of ∼9.6 MΩ. Assuming symmetric tunnel barriers, the lead-island resistances are, therefore, ∼4.8 MΩ. The HR device, however, has much higher resistances of ∼54 TΩ.

All our measurements are made at milli-Kelvin temperature in a dilution refrigerator with a magnetic field (400 mT) applied to suppress the superconductivity of the aluminum. The device is embedded in a radio frequency resonant circuit (Figure 1b), which comprises a chip inductor ($L = 470$ nH) and a parasitic capacitance ($C_p \sim 0.4$ pF). The circuit is placed in a reflectometry setup[17] and driven at resonance ($f_0 = 367.5$ MHz) by a small (≤ -95 dBm) carrier signal. The reflected
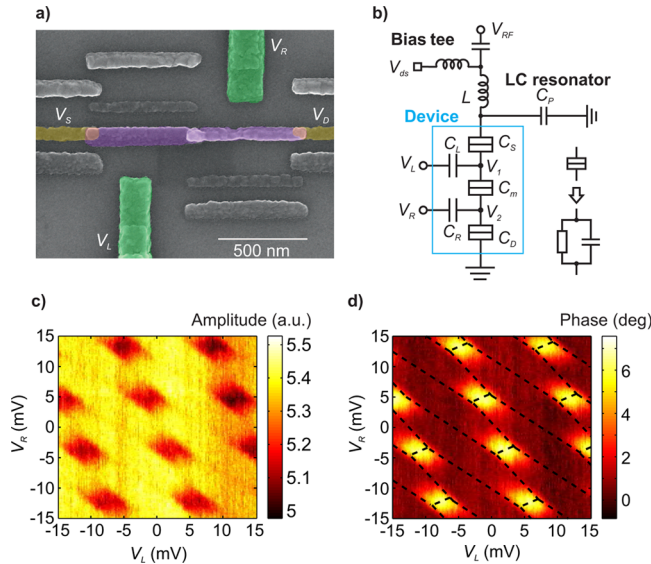
Figure 1. (a) False color SEM of the device, with source and drain leads (yellow; V_s and V_d) and electrostatic gates (green; V_R, V_L) highlighted. Islands are shown in purple. (b) Experimental wiring, with the equivalent circuit for the device embedded in a resonant circuit. A bias tee allows the application of a dc source-drain voltage (V_{ds}) in addition to the rf drive. (c) The amplitude of the reflected rf signal for the LR device as a function of V_L and V_R. For each column of (c) and (d), V_L is fixed, whereas V_R is swept and the average of 100 measurements taken. (d) The phase of the reflected signal as a function of V_L and V_R. Zero phase is chosen to be away from charge degeneracy points, and the boundaries of the charge stability diagram are highlighted.

Figure 2. (a) The amplitude of the reflected signal for the HR device as a function of V_L and V_R. (b) The phase of the reflected signal as a function of V_L and V_R. The boundaries of three cells of the charge stability diagram are highlighted. (c) Amplitude and phase along the crossection $A \rightarrow B$ averaged over 100 measurements. (d) Measured phase along the crossection $C \rightarrow D$ and phase calculated using the model described in the text.

signal is amplified at 4 K and room temperature, and its amplitude and phase are recorded.

We first present measurements on the LR device, showing amplitude (Figure 1c) and phase (Figure 1d) of the reflected rf signal as a function of gate potentials V_L and V_R. In Figure 1d, we highlight the honeycomb stability pattern characteristic of coupled double dots.[29] Each cell corresponds to a particular charge configuration of the double dot, which we label with an offset charge from an arbitrarily chosen (m, n) state. Close to the degeneracy between $(m + 1, n)$ and $(m, n + 1)$ charge states, it is possible for an electron to tunnel between islands in response to the rf drive. This leads to a Sisyphus impedance, and a change in both phase and amplitude is observed. At other charge state boundaries (for example, between (m, n) and $(m, n + 1)$), a much smaller Sisyphus impedance is seen because tunnelling is only weakly correlated with the rf drive due to the much larger resistance of the lead tunnel junctions.

We now describe measurements on the HR device. In Figure 2b, we show phase as a function of V_L and V_R, and highlight three charge state cells. We note that the sign of the phase shift induced by Z_S^{Im} is dependent upon the junction resistance and the rf drive frequency[22] and, here, is opposite to that for the LR sample. From the stability diagram and bias dependency measurements, we estimate the island charging energies to be $E_{c1} \approx E_{c2} \sim 240\ \mu eV$, and the electrostatic coupling energy to be $E_{cm} \sim 140\ \mu eV$.

To confirm the physical origin of the observed phase shift, we model the expected Sisyphus capacitance due to tunnelling through the middle junction. The effective capacitance between source and ground is $C = (dQ_S/dV_{ds})$, where $Q_s = C_s(V_{ds} - V_1)$ is the polarization charge on the source capacitance C_s, V_{ds} is
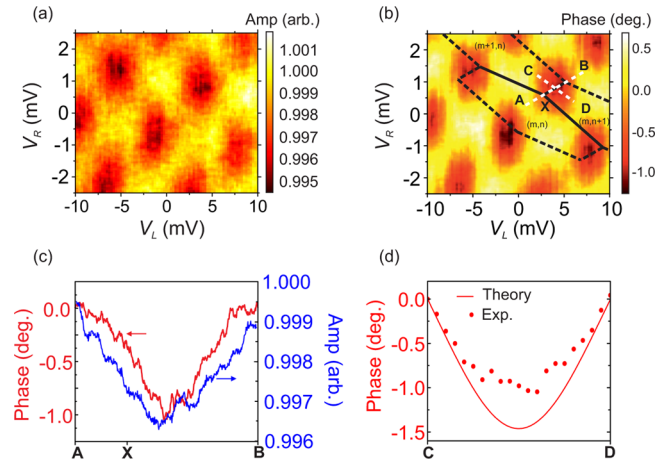
the source voltage, and V_1 is the voltage on the left island. In a two-island system, Q_s is found by solving the system of coupled equations

$$
\begin{aligned}
Q_1 &= C_S(V_{ds} - V_1) + C_m(V_2 - V_1) + C_L(V_L - V_1) \\
Q_2 &= C_m(V_1 - V_2) + C_R(V_R - V_2) - C_D V_2
\end{aligned}
\tag{1}
$$

where Q_1 and Q_2 are the charges on the left and right islands, respectively.

By solving eq 1 at the degeneracy between states $(n + 1, m)$ and $(n, m + 1)$, we find that the imaginary part of the Sisyphus impedance due to tunnelling between the left and right islands is $Z_S^{Im} = (((\omega C_S(C_2 - C_m))/(C_1 C_2 - C_m^2))(dQ_1/dV_{ds}))^{-1} = (((\omega C_S(C_2 - C_m))/(C_1 C_2 - C_m^2))((d\dot{Q}_1)/(dV_{ds}/dt)))^{-1}$. $d\dot{Q}_1$ is found by solving the master equation, as in ref 22, between states $(n + 1, m)$ and $(n, m + 1)$.

For the simulation, we use values of the capacitances deduced from the stability diagram, giving $C_S \approx C_R \sim 0.5\ fF$ and $C_m \sim 0.25\ fF$. From the S11 of the resonant circuit, we deduce a maximum phase shift of $1.45°$ at the degeneracy between $(n + 1, m)$ and $(n, m + 1)$, in agreement with the single shot data shown in Figure 3a. We also calculate the resultant phase along the line $C \rightarrow D$ in Figure 2b, which transects the degeneracy between the $(m + 1, n)$ and $(m, n + 1)$ charge states. This is shown in Figure 2d, and shows reasonable agreement with the experimental data. The discrepancy here can be attributed to the system spending a significant amount of time in excited states near the degeneracy point, which have a different Sisyphus impedance.

To probe the tunnelling dynamics of the device, we fix the gate voltages at a point close to the triple point between the (m, n), $(m + 1, n)$, and $(m, n + 1)$ charge regions and concentrate on the phase response. We then take a long (50 s) time trace. In Figure 3a, a typical trace segment is shown, for $V_{ds} = 0$ mV and $T = 35$ mK. We see a stochastic switching between two phases, separated by $1.4°$, corresponding to a change in $1/f_0$ Z_S^{Im} of 33 aF between the two states.

We attribute this impedance change to the thermally driven tunnelling of a single charge through the highly resistive tunnel
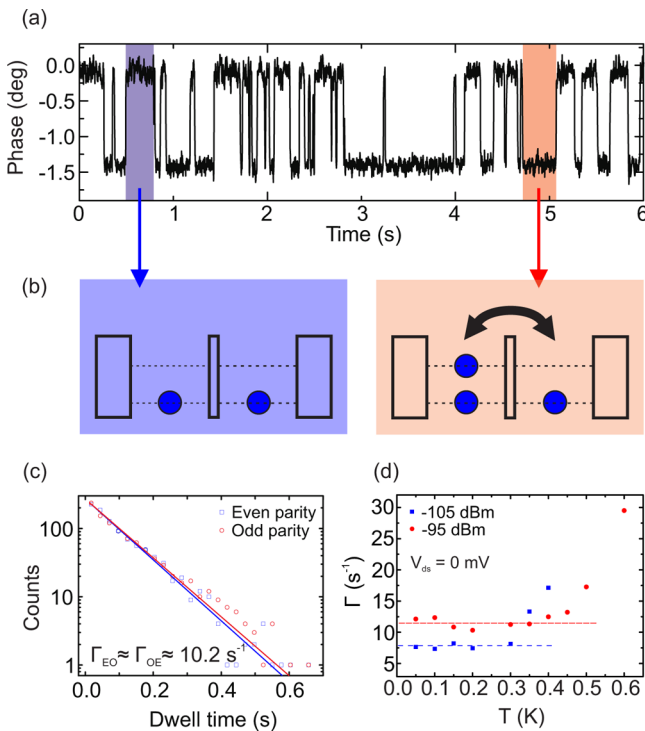
Figure 3. (a) Unaveraged phase close to the triple point (X) as a function of time. Stochastic switching is observed between states with an impedance contribution from Z_S^{Im} (blue region, left panel in b) and states where this contribution is not present (red region, right panel in b). (b) The Sisyphus process is blocked at even relative parity (left panel), where no excess electron is available, and present at odd relative parity (right panel), where an electron can tunnel between the two islands. (c) Histogram of dwell times for a long time trace at a triple point. We fit exponential distributions (solid lines) and determine both transition rates. (d) Dependence of rate on mixing chamber temperature for carrier powers of $P_{rf} = -105$ dBm (squares) and $P_{rf} = -95$ dBm (circles). The cycle rate saturates (dotted lines) at temperatures below the power dependent electron temperature.

junctions of the leads. When the device is in the (m, n) state (or other state with even parity relative to this state), the rf stimulus is unable to drive an electron through the middle junction, and so no Sisyphus impedance is observed (Figure 3b, left panel). The addition of an electron to the double island, however,

places the device in either the $(m + 1, n)$ or $(m, n + 1)$ state (or another odd relative parity state), and the Sisyphus impedance is now present due to the extra electron (Figure 3b, right panel).

To determine the tunnel rates of electrons on to and off of the device, a time trace is divided into "high" (where there is no Sisyphus impedance) and "low" (where the Sisyphus impedance is present) capacitance periods. The dwell times of these are determined, and they are then histogrammed (Figure 3c). We fit separate exponential decays and extract transition rates between the even and odd parity states, Γ_{EO} and Γ_{OE}. In general, the analysis of Poissonian transition rates requires the finite bandwidth of the measurement setup (in this case ~15 kHz) to be considered,[30] but here, we note that the measured rates are more than 2 orders of magnitudes lower than the bandwidth, and so this correction is negligible.

The average rate of parity change is given by $\Gamma = (1/2)(\Gamma_{EO} + \Gamma_{OE})$. In Figure 3d, we show Γ as a function of the temperature of the dilution fridge mixing chamber for two different rf carrier powers, with $V_{ds} = 0$. We observe a constant cycle rate for temperatures up to 250 mK ($P_{rf} = -105$ dBm) and 325 mK ($P_{rf} = -95$ dBm). At these temperatures, the electron temperature begins to increase and Γ, which is thermally driven, begins to rise. At lower rf powers and higher temperatures, the signal-to-noise ratio (SNR) degrades such that the two phase levels cannot be reliably distinguished.

We now quantify the behavior of the charge parity ammeter by measuring Γ as a function of V_{ds}. We show data at $T = 35$ mK and for two carrier powers (Figure 4). Two regimes can be identified. At low bias ($V_{ds} < 0.1$ mV) Γ is dominated by tunnelling events driven both thermally and by the rf carrier signal. The net charge flow in this regime is significantly less than $(1/2)e$. At higher bias ($V_{ds} > 0.2$ mV), events in which electrons are transferred from source to the device, or the device to the drain, dominate. This regime extends to lower bias for reduced carrier power.

We model this behavior by considering individual tunnel events onto and off the island pair. The tunnel rate through a single NIN junction is given by[31]

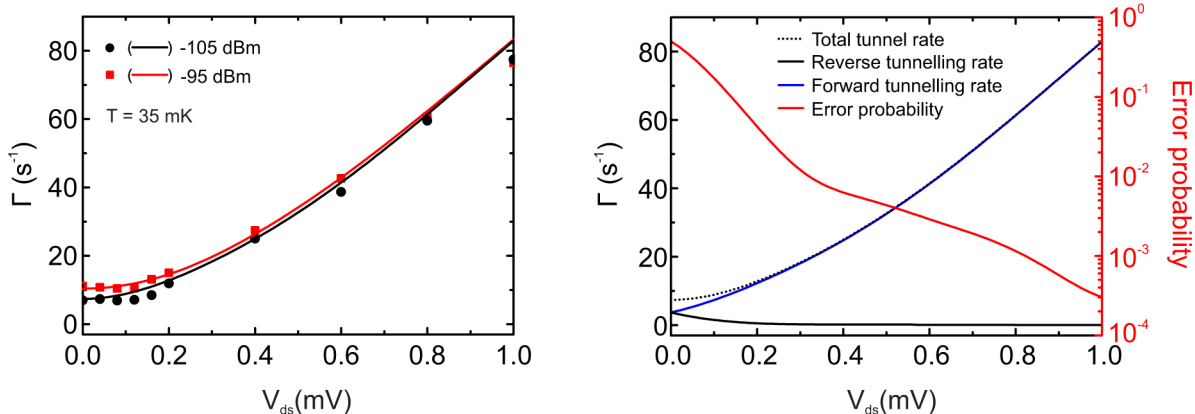$$\Gamma_t = \frac{R_k}{R_T} \frac{\Delta E/h}{1 - \exp(\Delta E/k_B T_E)}$$

Figure 4. (a) Dependence of cycle rate on drain-source bias for carrier powers of $P_{rf} = -105$ dBm (circles) and $P_{rf} = -95$ dBm (squares). The solid lines are fits to the model described in the text. (b) Components of the calculated rate for $P_{rf} = -105$ dBm in (a) as a function of drain-source bias. Forward (blue) and reverse (black solid) components of the total rate (black dots) are shown. The error probability $\Gamma_{reverse}/\Gamma_{total}$ is shown in red.

where ΔE is the change in chemical potential, $R_k = h/e^2$, and T_e is the electron temperature. There are two contributions to ΔE for each junction; a dc contribution, which includes V_{ds} and the chemical potential of the charge state involved, and an ac contribution from the rf drive. We include the rf drive by integrating the tunnel rate over one drive period and renormalizing. For forward transport

$$\Gamma_a = \frac{\omega}{2\pi} \frac{R_k}{R_t} \int_0^{2\pi/\omega} \frac{\Delta E(t)/h}{1 - \exp(\Delta E(t)/k_B T_E)} dt \qquad (2)$$

with $\Delta E(t) = (V_{rf}\sin(\omega t)+V_{dc})e$, and V_{rf} determined from the carrier power and Q factor of the resonant circuit.

To determine the rate of parity change for a given V_{ds} we solve the master equation for the double dot charge states to determine populations in each charge state. The total charge on the island can be increased (decreased) by the tunnelling of an electron from (to) either the source or drain. The rates for these processes are determined by solving eq 2 numerically for each state. The total rate of parity change is then given by the rate for each charge state weighted by the population of that state.

This description remains valid if a large source-drain bias such that $(eV_{ds} > E_c)$ is applied to the device, and it is therefore no longer in the Coulomb blockade regime. In this regime charge states other than (m, n), $(m + 1, n)$, and $(m, n + 1)$ can be occupied and the presence of the Sisyphus impedance depends upon the charge state being odd parity relative to (m, n). By measuring the phase shift, we monitor changes in the charge parity of the device in real time.

In Figure 4a we show a fit (solid lines) to the measured rates. The electron temperature is determined as above, and we find a good fit for resistances of 54 TΩ for each lead-island tunnel junction for both rf powers. These curves include parity changes due to tunnelling from both source and drain. In Figure 4b the forward and reverse components of the modeled rate for $P_{rf} = -105$ dBm are shown. We also show the error probability, defined as $\Gamma_{reverse}/\Gamma_{total}$, and we find that this drops approximately exponentially as V_{ds} increases. Therefore, at large V_{ds} almost all switches of parity are due to a net charge transfer of $(1/2)e$ from drain to source.

We measured $\Gamma_{EO,OE}$ tunnel rates in the range 10−100 Hz, corresponding to electrical currents of order aA. This demonstrates proof-of-principle of the charge parity ammeter, and we now discuss the prospects of measuring larger currents as required, for example, in current metrology. In our experiment, the rates were limited by the high lead-dot tunnel resistances and we could simply decrease these resistances to achieve higher currents. However, we cannot do this indefinitely, as the signal-to-noise ratio will start to limit measurable currents: as an example, we were not able to measure the discrete switching in the 5 MΩ LR device. From the data in Figure 2c, we find an SNR of 7.3 at a measurement bandwidth of 15 kHz. A sensitivity of 5.3×10^{-3} $e/(\text{Hz})^{1/2}$ is, therefore, implied for the present measurement.

There are ways to increase bandwidth: by using higher charging energy devices allowing a higher amplitude rf carrier signal, by optimizing the signal from the Sisyphus impedance, by using a lower noise temperature rf amplifier (at present $T_N = 10$ K), and by using a low-loss superconducting resonant circuit. With these modifications, it seems feasible to measure Γ in the MHz range, corresponding to pA electrical currents.

At low current levels, the current noise saturates at around 1.6 aA/$(\text{Hz})^{1/2}$. This compares favorably to typical values for room temperature preamplifiers of $\sim$5 fA/$(\text{Hz})^{1/2}$ (for example, SRS SR570 low noise current preamplifier, which has, however, a maximum bandwidth of 1 MHz.) Cryogenic preamplifiers limited by the Johnson noise of the source resistor have been demonstrated[32] with current noises of 1 fA/$(\text{Hz})^{1/2}$.

In conclusion, we have performed rf reflectometry measurements on a high resistance aluminum double dot. In measuring the electrical impedance of the device itself, we avoided the need for external charge detection in single electron ammetery and could directly determine the relative charge parity of a metal double dot. This configuration benefits from simplicity in the design and also is well suited to the use of high bandwidth electrical techniques, in principle enabling relatively large currents to be measured. We also avoid problems that may arise due to the back action from charge sensors. Although the requirement for finite V_{ds} to avoid miscounts due to charges transferring from drain to source is in contrast to the zero bias drop across an ideal ammeter, the charging energy of nodes in single electron circuits can reach several tens of meV, at least an order of magnitude above the bias range explored here.

A related charge parity measurement has application in measuring the spin state of semiconductor quantum dots.[27]

■ AUTHOR INFORMATION
Corresponding Authors
*N. J. Lambert. E-mail: nl249@cam.ac.uk.
*A. J. Ferguson. E-mail: ajf1006@cam.ac.uk.
Notes
The authors declare no competing financial interest.

■ REFERENCES
(1) Bylander, J.; Duty, T.; Delsing, P. *Nature* **2004**, *434*, 9.
(2) Lu, W.; Ji, Z.; Pfeiffer, L.; West, K. W.; Rimberg, A. J. *Nature* **2003**, *423*, 422−5.
(3) Güttinger, J.; Seif, J.; Stampfer, C.; Capelli, A.; Ensslin, K.; Ihn, T. *Phys. Rev. B* **2011**, *83*.
(4) Keller, M. W. *Metrologia* **2008**, *45*, 102−109.
(5) Giblin, S. P.; Wright, S. J.; Fletcher, J. D.; Kataoka, M.; Pepper, M.; Janssen, T. J. B. M.; Ritchie, D. A.; Nicoll, C. A.; Anderson, D.; Jones, G. A. C. *New J. Phys.* **2010**, *12*, 073013.
(6) Keller, M. W.; Martinis, J. M.; Zimmerman, N. M.; Steinbach, A. H. *Appl. Phys. Lett.* **1996**, *69*, 1804.
(7) Yamahata, G.; Nishiguchi, K.; Fujiwara, A. *Appl. Phys. Lett.* **2011**, *98*, 222104.
(8) Giblin, S. P.; Kataoka, M.; Fletcher, J. D.; See, P.; Janssen, T. J. B. M.; Griffiths, J. P.; Jones, G. A. C.; Farrer, I.; Ritchie, D. A. *Nat. Commun.* **2012**, *3*, 930.
(9) Pekola, J. P.; Saira, O.-P.; Maisi, V. F.; Kemppinen, A.; Möttönen, M.; Pashkin, Y. a.; Averin, D. V. *Rev. Mod. Phys.* **2013**, *85*, 1421−1472.
(10) Fricke, L.; Hohls, F.; Ubbelohde, N.; Kaestner, B.; Kashcheyevs, V.; Leicht, C.; Mirovsky, P.; Pierz, K.; Schumacher, H. W.; Haug, R. J. *Phys. Rev. B* **2011**, *83*, 193306.
(11) Fricke, L.; Wulf, M.; Kaestner, B.; Kashcheyevs, V.; Timoshenko, J.; Nazarov, P.; Hohls, F.; Mirovsky, P.; Mackrodt, B.; Dolata, R.; Weimann, T.; Pierz, K.; Schumacher, H. W. *Phys. Rev. Lett.* **2013**, *110*, 126803.
(12) Wulf, M. *Phys. Rev. B* **2013**, *87*, 035312.

(13) Fujisawa, T.; Hayashi, T.; Hirayama, Y.; Cheong, H. D.; Jeong, Y. H. *Appl. Phys. Lett.* **2004**, *84*, 2343.

(14) Schleser, R.; Ruh, E.; Ihn, T.; Ensslin, K.; Driscoll, D. C.; Gossard, A. C. *Appl. Phys. Lett.* **2004**, *85*, 2005.

(15) Vandersypen, L. M. K.; Elzerman, J. M.; Schouten, R. N.; Willems Van Beveren, L. H.; Hanson, R.; Kouwenhoven, L. P. *Appl. Phys. Lett.* **2004**, *85*, 4394.

(16) Gustavsson, S.; Shorubalko, I.; Leturcq, R.; Schön, S.; Ensslin, K. *Appl. Phys. Lett.* **2007**, *92*, 152101.

(17) Schoelkopf, R. J.; Wahlgren, P.; Kozhevnikov, A. A.; Delsing, P. *Science* **1998**, *280*, 1238−1242.

(18) Qin, H.; Williams, D. A. *Appl. Phys. Lett.* **2006**, *88*, 203506.

(19) Reilly, D. J.; Marcus, C. M.; Hanson, M. P.; Gossard, A. C. *Appl. Phys. Lett.* **2007**, *91*, 162101.

(20) Fujisawa, T.; Hayashi, T.; Tomita, R.; Hirayama, Y. *Science* **2006**, *312*, 1634−1636.

(21) Persson, F.; Wilson, C. M.; Sandberg, M.; Johansson, G.; Delsing, P. *Nano Lett.* **2010**, *10*, 953−7.

(22) Ciccarelli, C.; Ferguson, A. J. *New J. Phys.* **2011**, *13*, 093015.

(23) Ota, T.; Hayashi, T.; Muraki, K.; Fujisawa, T. *Appl. Phys. Lett.* **2010**, *96*, 032104.

(24) Ashoori, R. C.; Stormer, H. L.; Weiner, J. S.; Pfeiffer, L. N.; Pearton, S. J.; Baldwin, K. W.; West, K. W. *Phys. Rev. Lett.* **1992**, *68*, 3088−3091.

(25) Duty, T.; Johansson, G.; Bladh, K.; Gunnarsson, D.; Wilson, C.; Delsing, P. *Phys. Rev. Lett.* **2005**, *95*.

(26) Petersson, K. D.; Smith, C. G.; Anderson, D.; Atkinson, P.; Jones, G. A. C.; Ritchie, D. A. *Nano Lett.* **2010**, *10*, 2789−93.

(27) Schroer, M. D.; Jung, M.; Petersson, K. D.; Petta, J. R. *Phys. Rev. Lett.* **2012**, *109*, 166804.

(28) Fulton, T.; Dolan, G. *Phys. Rev. Lett.* **1987**, *59*, 109−112.

(29) van der Wiel, W.; De Franceschi, S.; Elzerman, J. M.; Fujisawa, T.; Tarucha, S.; Kouwenhoven, L. P. *Rev. Mod. Phys.* **2002**, *75*, 32.

(30) Naaman, O.; Aumentado, J. *Phys. Rev. B* **2006**, *73*, 4.

(31) Grabert, H.; Devoret, M. H. *Single charge tunneling: Coulomb blockade phenomena in nanostructures*; Plenum Press: New York, 1992.

(32) Yvon, D.; Sushkov, V.; Bernard, R.; Bret, J.; Cahan, B.; Cloue, O.; Maillard, O.; Mazeau, B.; Passerieux, J.; Paul, B.; Veyssiere, C. *Nucl. Instrum. Methods Phys. Res., Sect. A* **2002**, *481*, 306−316.